Electrical Power and Energy Systems 155 (2024) 109600

Contents lists available at ScienceDirect

International Journal of Electrical Power and Energy Systems

journal homepage: www.elsevier.com/locate/ijepes

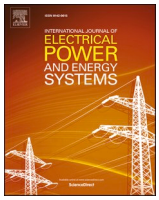

Hierarchical bi-level load frequency control for multi-area interconnected power systems

Abdullahi Bala Kunya

Department of Electrical Engineering, Ahmadu Bello University, Zaria, Nigeria

ARTICLE INFO

Keywords:
Control area
Linear quadratic regulator
Load frequency control
Multi area power systems
Tie-line power
Moth flame optimization

ABSTRACT

To overcome the shortcomings of proportional–integral (PI) control, a linear quadratic regulator (LQR) is proposed in this study, to determine the set points of the PI controllers in a two-level hierarchical manner. The application of the proposed scheme is studied on load frequency control (LFC) of a power system with multiple control areas (CAs). At the lower control level, a discrete PI controllers are used to regulate the frequency and tie-line powers of each of the CAs. To achieve an improved closed loop performance, the local PI controllers are optimally tuned using moth flame optimization (MFO) algorithm by minimizing the Integral Square Error (ISE) of the state errors with respect to local information and interactions with neighboring CAs. While at the upper control layer, an optimized finite-horizon LQR is applied as a guide to establish the optimal set-points of the lower level PI controllers. Since only few of the state variables can be accessed, Kalman filter (KF) is applied as an observer for the estimation of the remaining states. The efficacy of the proposed scheme is verified by implementing it on a three-CA system perturbed with a step and random net disturbances formed by combining the fluctuations in the output power of DFIG-based wind turbine generator and random load demand. From the simulation results, it is established that the proposed LQR-PI supervisory scheme has outperformed the conventional PI control scheme in optimality and stability.

1. Introduction

Owing to the stringent requirement of uninterrupted balance in active power generation and demand, secondary control better known as load frequency control (LFC), is the most perplexing task in the control of power system. Mismatch in generation-demand balance deteriorates the system performance severely via incessant variations in the tie-line power, frequency and voltage levels, among others. The severity of the deterioration worsens if the PS has multiple control areas (CA) due to the increased nonlinearities of the system [31,18]. A small perturbation in generation-demand balance in one CA of the MAPS can lead to frequency deviation in that particular CA as well as its neighbors. Active load disturbance is the major cause of generation-demand mismatch as such electrical power generation is carefully monitored [8,35]. In addition, fluctuations in the output power of renewable energy sources (RES) also contribute. The mismatch is originally resolved by instant extraction of kinetic energy at the detriment of system frequency. Unless the generation-demand balance is regained, the frequency and tie-line powers keep deviating from the corresponding nominal values [42,4]. If these undesirable deviations persist, the system generators (mostly synchronous) no longer be coherent, hence the system collapses. To restrain the consequences of the generation-demand mismatch, LFC is applied. It is applied to optimally regulate the power generation as the demand fluctuates, with the aim of keeping the frequency and inter-CA powers within the allowable predefined ranges [13,6]. Earlier frequency control schemes use flyballs to activate a hydraulic system for adjusting the throttle valves of the system prime movers. Modern generators use electronic governors to accomplish the same task [48,41].

There are numerous research works carried out on LFC, which mainly applied modern optimal control [34,24], adaptive and sliding model variable structure methods [2,49], robust approaches [16;5], and intelligent approaches[29,27]. While some studies applied classical control such as PI in [1,39] and PID controllers [20,9]. This family of

Abbreviations: ACE, Area Control Error; CA, Control areas; EVs, Electric vehicle; GDB, Governor dead band; HVDC, High voltage direct current; ISE, Integral square error; ITAE, Integral of time by absolute value of error; KF, Kalman filter; LFC, Load frequency control; LQR, Linear quadratic regulator; MAP, Multi-area power system; MFO, Moth Flame Optimization; MG, Micro-grid; PI, Proportional integral; PID, Proportional integral derivative; QO, quasi-oppositional; RES, Renewable energy sources; SCADA, Supervisory Control and Data Acquisition; WAMS, Wide Area Measurement System; WT, Wind turbine.

E-mail address: abkunya@abu.edu.ng.

https://doi.org/10.1016/j.ijepes.2023.109600
Received 4 February 2023; Received in revised form 15 July 2023; Accepted 17 October 2023
Available online 8 November 2023

controllers has been applied widely not only for LFC application but control of other dynamic systems, largely owing to the simplicity of the concept and ease of implementation. However, the robustness of classical controllers worsens greatly with the increase in the system nonlinearities [32]. As such, numerous studies paid considerable attention to improve their robustness and stability. Application of Grey Wolf Optimization is demonstrated in [37] for LFC in MAPS based on the minimization of the Integral of Time Multiplied by Absolute Value of Error (ITAE) of the some selected states. Likewise in [39], a dual-mode PI controller applied for frequency regulation is tuned using whale optimization algorithm (WOA). The speed, efficiency and reliability of the controller is enhanced by incorporating the WOA with quasi-oppositional (QO) learning theory. Similar approach is presented in [7], however a QO differential search algorithm is used in place of the WOA. An improved differential evolution algorithm tuned fuzzy PID controller is presented in [29]. To improve its performance, the controller is reinforced with thyristor-controlled series compensator.

In a similar study, application of fuzzy PI controller for frequency control of a linear and nonlinear MAPS is investigated in [33]. The gain of the controller in tuned using Jaya optimization algorithm with and without the effect of governor dead band. In [24], same algorithm is applied to tune a fuzzy controller online for LFC of WT integrated MAPS.

Moreover, robust control techniques such as sliding mode control, model predictive control (MPC) [5,12,6], linear quadratic regulator (LQR) [11,28], fuzzy controller [24,3,30] and hybrid of these schemes [22,25]were proposed. For instance, coordination-based distributed MPC is applied for frequency control of 4-CA MAPS with wind turbine (WT) in [48]. The scheme is designed to lessen the effect of the intermittency of wind speed. Also in [5], distributed MPC is applied for LFC in a deregulated MAPS using output feedback, in which distributed observers estimate the inaccessible states and disturbances for the local controllers. While in [43], a multi-objective MPC in enhanced with Dynamic Adaptability functionality and applied for frequency regulation of grid-tied inverter based micro-grid (MG). Frequency regulation of MAPS with high penetration of DGs is presented in [45]. The frequency regulation problem is expressed as a predictive control problem. An algorithm based on distributed projection by means of peer-to-peer communication is then proposed for its solution. LFC in a restructured MAPS using LQR controller is presented [36]. Impact of high voltage direct current (HVDC) tie-line on LFC is also investigated in the study. However, in most of these reviewed studies, the system state variables are assumed to be measurable and noise-free, which is always hypothetical. Hence the need for a state observer arises.

Furthermore, in [25], generalized extended state observer (GESO) and an SMC with nonlinearities are used as hybrid to investigate the LFC in MAPS. In the study, the GESO is employed to estimate the state and disturbance and at the same time rejecting the disturbance in the MAPS.

Unlike the control schemes discussed above employing single controller for the LFC, in some works, multiple controllers are combined. In [10], robust H_2 and H_∞ controllers are mixed and synthesized via iterative linear matrix inequality for LFC in MAPS with electric vehicle (EVs). Uncertainties associated with EV dispatch capacity and time delay linked to their charging/discharging control as relate to LFC were also investigate. In [44], LFC is proposed using two MPC controllers cascaded to form double layer control scheme. Economic MPC is applied in the upper for optimized power sharing among the LFC units in the areas, while in the lower layer distributed MPC is applied to actualize the LFC. In similar works [27,38], a double layer control scheme based on optimal robust controller is designed for LFC application. The double level control architecture is to ensure optimal solution for LFC and lessen the computational burden on the controllers. Likewise, [26]applied same technique but interactions between neighboring areas are considered. A multi-agent based synchronized control scheme with two control layers is presented in [46]. Cascading these controllers have improved the close loop performance of the LFC generally, however it is at the detriment of the computational time and computer memory.

In this study, a hierarchical control strategy is applied for LFC for interconnected MAPS. In the lower control level, discrete PI controllers are used to normalize the frequencies and tie-line powers, while at the upper control layer, an LQR is applied as a supervisory regulator to optimally determine the set-points of the PI controllers in the lower level. To improve the performance of the scheme, moth flame optimization (MFO) is applied to optimally tune the controllers at the lower control layer based on the Integral Square Error (ISE) of the state errors with respect to local information and interactions with neighboring CAs, subject to system dynamic constraints. The key contributions of the study are itemized as: -.

i- Proposing a supervisory LQR-PI load frequency control of MAPS. The coordination between the two controllers has the robustness of the PI controllers while leveraging the optimal control capabilities of the LQR.
ii- Proposing an LFC scheme capable of handling step and random load disturbances with reduced control effort. The upper layer LQR optimizes the control actions by considering the system's dynamics, while the lower level PI controller provides integral action to handle steady-state errors and minimize the control effort.
iii- Demonstrates the application of KF for the estimation of inaccessible states of the system based on the measurable ones. In addition, the KF covariance matrices are adjusted based on the continuous variation of the measurement noise.

After this introductory section, the remaining part of the paper is arranged with the formulation of the proposed LFC architecture presented in Section 2, while Section 3 presenting the control levels design and robustness analysis. Section 4 discusses the simulation results and the conclusion followed in Section 5.

2. Proposed LFC architecture

This section present the control architecture of the proposed LFC scheme.

2.1. Multi-area system load frequency control

Power system network is a non-linear dynamic system, however its model is often linearized [13]. The linearization only alter the physical representation of the system slightly and LFC operation is characterized by small system perturbation. For these reasons, linearized MAPS modelled in state-space representation is used in this study.

The formulation of the model is centered at differential equations describing the dynamics of the individual components of the MAPS like tie-line powers, governor and turbine dynamics, among others. Fig. 1 shows the transfer function representation of a CA in a typical MAPS with thermal power plants.

From the block diagram depicting the dynamic model of the CA, the state space model can be derived distinctively.

The frequency deviation, Δf_i is formulated from a linearized *swing equation* shown in (1) [5].

$$\frac{d\Delta f_i}{dt} = \frac{1}{M_i}\left(P_i^G - D_i f_i - P_i^{tie} - P_i^{net}\right) \tag{1}$$

Where P_i^{net} is the net disturbance formed by taking the resultant effects of the sources of disturbance in the ith CA as expressed in (2),

$$P_i^{net} = P_i^D - P_i^{ren} \tag{2}$$

The main sources of disturbance are the changes in the active load and fluctuations in the output power of renewable energy sources (RES), P_i^{ren}.

M_i represents the ith CA net inertia constant. It defines the

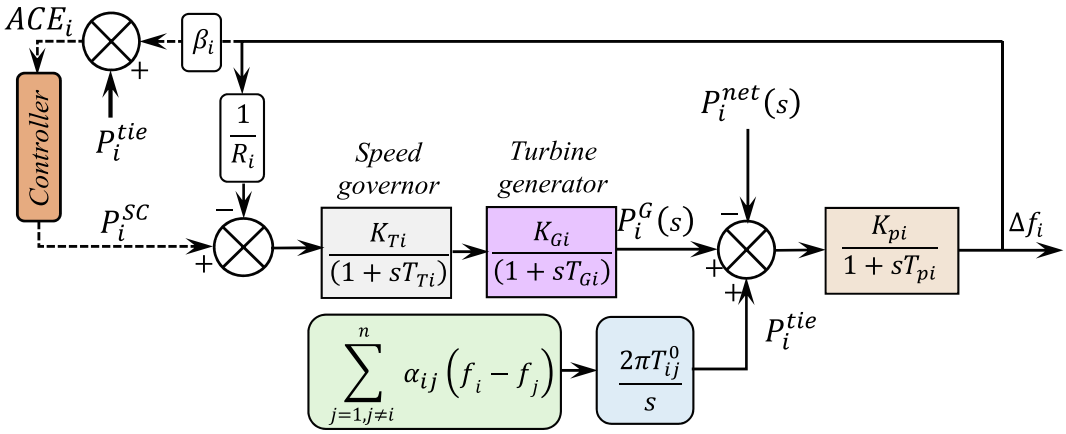

Fig. 1. Transfer function representation of *i*th CA in a typical MAPS with thermal power plant.

characteristic value for each synchronous machine in each CA. With the assumption that generators in that area form a coherent group, it is acceptable to define a single frequency for each area.

Not all the generators in the system participate in LFC. Only generators providing spinning reserve at a particular time are engaged in LFC, which for security consideration, are often scheduled hours ahead. As modelled in (3), the generation from this set of generators are added up as CA aggregate generation, P_i^G [14].

$$P_i^G = \sum_{j=1}^{G} P_{i,j}^G; \tag{3}$$

In regulated MAPS with vertically integrated utility, each CA is expected to cater for its loads thereby limiting inflow of power from neighboring CAs. However, in deregulated system, a distribution company in one CA can purchase power from a generation company in another CA via transmission system operator. The MAPS in this study has regulated structure, hence the tie-line power model is obtained considering all the power exchanges with the neighboring areas, as in (4).

$$\frac{dP_i^{tie}}{dt} = \sum \dot{P}_{ij} where \frac{dP_{ij}}{dt} = 2\pi W_{ij}^0(\Delta f_i - \Delta f_j) \tag{4}$$

Where W_{ij}^0 is the synchronizing coefficient which depends on the static transmission capacity of *ij*th line. In real MAPS, CAs have different MVA rating, hence α_{ij} defines the ratio of the rated capacities of *i*th and *j*th CAs as shown in (5).

$$P_{ji} = -\frac{P_{MVA_i}}{P_{MVA_j}} P_{ij} = -\alpha_{ij} P_{ij} \tag{5}$$

The system frequency is adjusted by varying the set point of the turbine. Assuming a slight perturbation in the system, the dynamics of *g* th turbine in the *i*th CA is modelled as (6);

$$\frac{dP_{i,g}^G}{dt} = sat_{P_{i,g}^G}^i \left\{ \frac{1}{T_{T_{i,g}}} \left(P_{i,g}^{Gov} - P_{i,g}^G \right) \right\} \tag{6}$$

To adjust the set point of each generator turbine, a supplementary optimal control signal,P_i^{sc} obtained from the LFC controller is used. Since the set points cannot be adjusted instantly, additional state is added to model as speed governor. The adjustment in the governor valve position, as a function of frequency deviation is expressed in (7) [25],

$$\frac{dP_{i,g}^{Gov}}{dt} = \frac{1}{T_{Gov_{i,g}}} \left(P_{i,g}^{sc} - P_{i,g}^{Gov} - \frac{1}{R_{i,g}} \Delta f_i \right) \tag{7}$$

The *i*th Area Control Error (ACE) is formulated by summing up the deviations Δf_i and P_i^{tie}, as defined in (8) [5]. The ACE forms the feedback input signal to the LFC controller as shown in Fig. 1.

$$\mathrm{ACE}_i = \beta_i \Delta f_i + P_i^{tie} \tag{8}$$

The LFC controller then compute the $P_{i,g}^{sc}$ based on certain control law at a predefined time interval. Other symbols used in the modelling are summarized in Table 1.

The modelling equations in (1) – (8) defining the state variables are rearranged to a standard state-space of form (9) as shown in (10) and (11);

$$\begin{cases} \dot{x}_i(t) = A_i x_i(t) + B_i u_i(t) + E_i d_i^{int}(t) + F_i d_i^{ext}(t) \\ y_i(t) = C_{ii} x_i(t) \end{cases} \tag{9}$$

$$\frac{d}{dt}\begin{bmatrix} \Delta f_i \\ P_{i,g}^G \\ P_{i,g}^{Gov} \\ P_i^{tie} \end{bmatrix} = \begin{bmatrix} -\frac{D_i}{M_i} & \frac{1}{M_i} & 0 & -\frac{1}{M_i} \\ 0 & -\frac{1}{T_{T_{i,g}}} & \frac{1}{T_{T_{i,g}}} & 0 \\ -\frac{1}{R_{i,g} T_{Gov_{i,g}}} & 0 & -\frac{1}{T_{Gov_{i,g}}} & 0 \\ \sum_{j \in \mathscr{A}_i^{tie}} 2\pi W_{ij}^0 & 0 & 0 & 0 \end{bmatrix} \begin{bmatrix} \Delta f_i \\ P_{i,g}^G \\ P_{i,g}^{Gov} \\ P_i^{tie} \end{bmatrix} + \begin{bmatrix} 0 \\ 0 \\ \frac{1}{T_{Gov_{i,g}}} \\ 0 \end{bmatrix} P_{i,g}^{sc} + \begin{bmatrix} -\frac{1}{M_i} \\ 0 \\ 0 \\ 0 \end{bmatrix} P_i^{net} + \begin{bmatrix} -\frac{1}{M_i} \\ 0 \\ 0 \\ -2\pi \sum_{j \in \mathscr{A}_i^{tie}} W_{ij}^0 \end{bmatrix} \Delta f_j \tag{10}$$

$$\mathrm{ACE}_i = \begin{pmatrix} \beta_i & 0 & 0 & 1 \end{pmatrix} \begin{pmatrix} \Delta f_i & P_{i,g}^G & P_{i,g}^{Gov} & P_i^{tie} \end{pmatrix}^T \tag{11}$$

The state vector, x_i is defined as $\begin{bmatrix} \Delta f_i & P_{i,g}^G & P_{i,g}^{Gov} & P_i^{tie} \end{bmatrix}^T \in \mathbb{R}^4$ is the state vector, $u_i = P_{i,}^{sc}$ is the supplementary control signal, $d_i^{int} = P_i^{net}$ is the system disturbance within the CA, while $d_i^{ext} = \Delta f_j$ is the disturbance attributed to frequency deviations from neighboring CAs and $\mathrm{ACE}_i : \forall i = 1, 2, \cdots n$ is the system output.

2.1.1. Propose hierarchical LFC structure

A two-level hierarchical LFC scheme of 3-area MAPS is proposed in this work. A discrete PI controllers are used at lower level to control the frequency and tie-line powers, while at the upper control layer, an

Table 1
System terminologies.

Symbol	Description
Δf_i	Frequency deviation ith area [Hz].
$P^G_{i,m}$	Change in mth generation in ith area [MW].
P^{tie}_i	Change in net tie-line power in ith area [MW].
D_i	ith CA damping coefficient [MW/Hz].
P^D_i	Change in ith area active demand [MW].
β_i	Frequency bias constant for ith area [MW/Hz]
P^{ren}_i	Fluctuations in RES output power in ith area [MW]
$R_{i,m}$	Droop parameter of mth unit in the ith area, [MW/Hz].
P_{MVA_i}	MVA rating of ith CA
α_{ij}	Ratio of ith to jth CA in the MAPS
$T_{Gov_{i,m}}$	Governor time constant of generator m in the ith area.
$T_{T_{i,m}}$	Turbine time constant of mth of ith area.
$\mathscr{A}^{tie}_i$	Index set of areas interconnected to ith area.

optimized LQR is applied as a supervisory regulator to establish the optimal set-points of the controllers in the lower level as shown in Fig. 2.

The developed supervisory LQR will be designed to compute the optimal set-points so as to coordinate decentralized control actions of the local PIs. The scheme is developed to overcome the general drawback of PI controllers like handling the uncertainties and nonlinearities in the system and the integrator windup.

Unlike centralized control which presents lots of reliability and instability problems when the central controller or the communication links malfunction, the proposed control scheme continue to operate albeit failure happens in the higher control level. The PIs in the lower level get their reference set points from a preset value in the Wide Area Measurement System (WAMS). WAMS model is used in this paper instead of Supervisory Control and Data Acquisition (SCADA) due to difficulty in the implementation of SCADA in real MAPS. SCADA measures only the steady state information of the system asynchronously, while WAMS equipped with PMUs and GPS systems enable synchronous monitoring of MAPS dynamics in a precise time scale and sampling.

3. Design of the control scheme

The design of the two control levels is presented in this section.

3.1. Higher control layer

The higher control level comprises of an LQR, applied to optimal set the reference for the PI controllers at the lower level as discussed in subsection 2A. The LQR is designed to compute the set-points so as to provide a coordinated control actions of the decentralized local PIs. The coordination between the two levels is somewhat similar to the switching of multi-source system presented in [23].

3.1.1. Kalman filter

To apply an LQR for the control of a dynamic system, all the state variables must be available and noise-free. However, not all the states of real dynamic systems like MAPS are measurable neither noise-free [36]. Hence, Kalman filter (KF) is applied as the observer for the estimation of the inaccessible state variables. It estimates the states based on the measurable ones such as frequency and tie-line powers and their respective deviations notwithstanding the measurement noise (ξ) and the process noise (ψ).

The state space model in (9) defining the system dynamics, is remodeled to include the noises in the system, as

$$\begin{cases} \dot{x}_i(t) = A_i x_i(t) + B_i u_i(t) + E_i^{'} d_i(t) + V_i \psi_i(t) \\ y_i(t) = C_{ii} x_i(t) + W_i \xi_i(t) \end{cases} \tag{12}$$

Where d_i represents system disturbances originated within and outside ith CA. It is assumed that the noise vectors have zero averages and are mutually independent. As such, the vectors and their respective covariance matrices, Q_{kf} and R_{kf} can be expressed as;

$$\begin{cases} Q_{kf} = \mathrm{E}\{\psi_i(t)\psi_i{}^T(t)\} \geq 0 \forall i = 1, 2, \cdots, n \\ R_{kf} = \mathrm{E}\{\xi_i(t)\xi_i{}^T(t)\} > 0 \forall i = 1, 2, \cdots, n \\ \mathrm{E}\{\psi_i(t)\xi_i{}^T(t)\} = 0 \forall i = 1, 2, \cdots, n \end{cases} \tag{13}$$

The KF is adjusted based on an index defined in (14), as a function of the estimated state variables ($\widetilde{x}_i$), so as to improve the closed loop performance.

$$I_i(t) = \lim_{t\to\infty} \mathrm{E}\left\{ \left(x_i(t) - \widetilde{x}_i(t) \right)^T C_{ii}{}^T C_{ii} \left(x_i(t) - \widetilde{x}_i(t) \right) \right\} \tag{14}$$

With the estimated states and output of the ith CA ($\widetilde{y}_i$), the state space model for the KF is augmented as:

$$\begin{cases} \dot{\widetilde{x}}_i(t) = A_i \widetilde{x}_i(t) + K_{kf} \left(y_i(t) - \widetilde{y}_i(t) \right) \\ \widetilde{y}_i(t) = C_{ii} \widetilde{x}_i(t) \end{cases} \tag{15}$$

K_{kf} is the KF gain calculated from one the solution of the Filter Algebraic Riccati Equation, expressed in (16).

$$\lambda_{kf} A_i{}^T + A_i \lambda_{kf} + \psi_i{}^T Q_{kf} \psi_i - \lambda_{kf} C_{ii}{}^T \delta C_{ii} \lambda_{kf} = 0 \tag{16}$$

Then the gain is calculated using

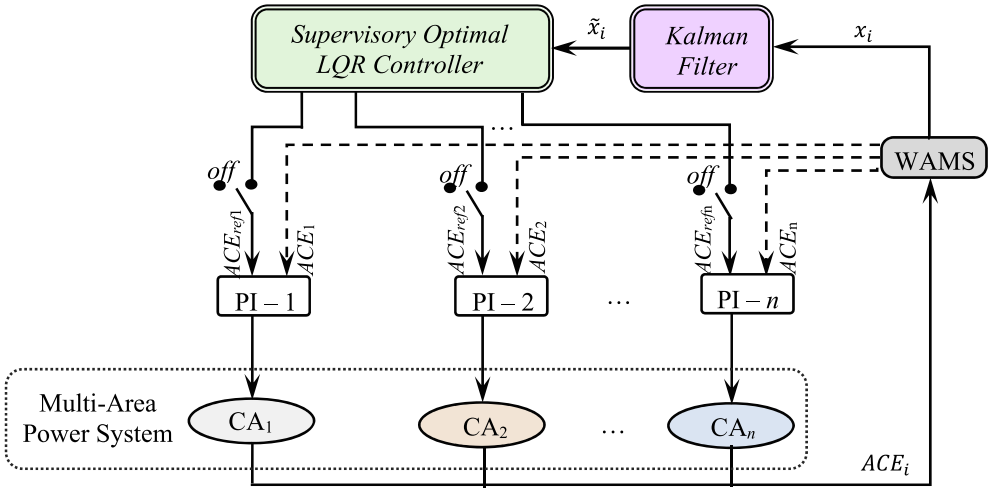

Fig. 2. Architecture of the proposed system.

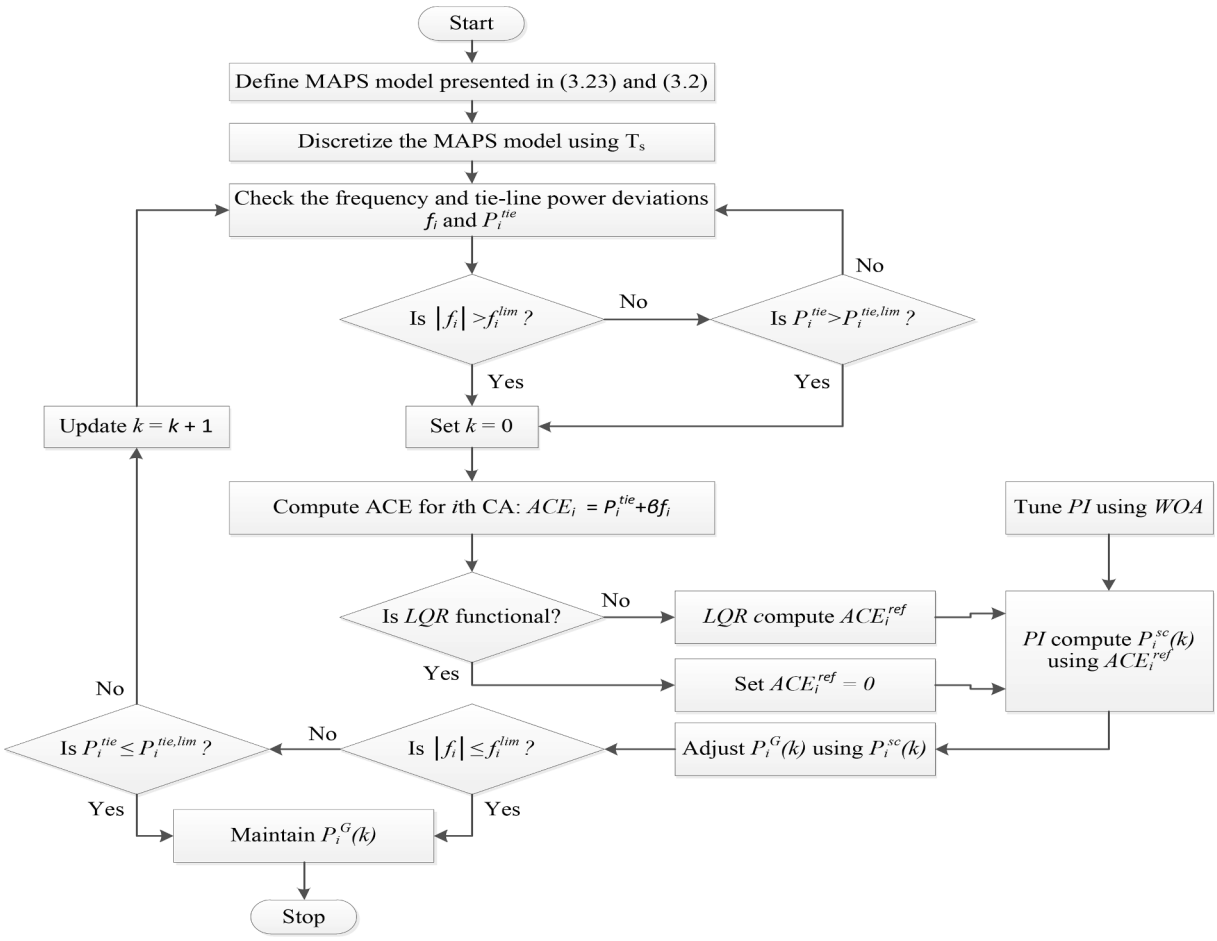

Fig. 3. Flowchart of the Proposed LQR-PI Load Frequency Control.

$$K_{kf} = \lambda_{kf} C_{ii}^{\ T} \delta \tag{17}$$

3.1.2. LQR controller

The LQR controller uses the states (measured and those estimated by the KF) and generate the optimal feedback control input to the lower level decentralized PI (dec-PI) controllers, based on a state feedback gain "*K*" which is often optimized. The feedback control law shown in (18) obtained by minimizing (17), is applied to obtain the gain, *K*.

$$u(t) = -K(t)x_i(t) \tag{18}$$

The LQR problem is to search for the finite future optimal control moves to minimize the cost function depicted in (19),

$\underset{u(t)}{minJ}$ Such that

$$J = \int_{t_0}^{t_f} \left(\tilde{x}_i(t)\right)^T Q \tilde{x}_i(t) + \int_{t_0}^{t_f} \left(u_i^{ref}(t)\right)^T R u_i^{ref}(t) \tag{19}$$

Where $\boldsymbol{Q} \in \mathbb{R}^{n_i \times n_i}$ is positive semi-definite matrix, as such all its principle minors are non-negative. While $\boldsymbol{R} \in \mathbb{R}^{n_i \times n_i}$ is a real symmetric matrix. The selection of the elements of Q and R makes it possible to relatively weigh the state variables and the respective control inputs [45]. Even though the matrices can be chosen arbitrarily [19] or through eigenvalue analysis [40], in this research, they are chosen carefully to provide a trade-off between control effort and system performance. The matrices are chosen as $Q = diag(9.6 \quad 1.4 \quad 1.2 \quad 9.6)$ and $R = diag(1.1 \quad 0.9 \quad 0.9 \quad 1.1)$.

3.1.3. Controllability and stabilizability analysis

For KF to be applied, the system must be controllable and observable.

Controllability of a system defines the probability of constraining the system to a certain state when a control input is applied. Thus, where a state is uncontrollable, it implies that the input capable of controlling that state does not exist.

Consider the simplified *n*-dimensional form of (9),

$$\begin{cases} \dot{x}(t) = Ax(t) + Bu(t) \\ \quad y(t) = Cx(t) \end{cases} t \in (t_0, \infty) \tag{20}$$

Where $A \in \mathbb{R}^{n \times n}$, $B \in \mathbb{R}^{n \times m}$, $C \in \mathbb{R}^{1 \times n}$,

Definition 1. (State Controllability): The state equation (20) is considered to be completely state controllable if for any initial state, $x(t_0)$ and any final state, $x(t_N)$, there exists an input sequence $u(t_0)$, $u(t_1)$,.., $u(t_N)$, which transfers $x(t_0)$ to $x(t_N)$, for some finite N. Otherwise the system is state uncontrollable.

Definition 2. (Controllability): The system (20) is controllable on an interval $[t_0; t_1]$ if $\forall\ x_0, x_1 \in \mathbb{R}^n$; $\exists$ controllable function $u \in L^2([t_0; t_1] : \mathbb{R}^m)$ such that the corresponding solution of (20) satisfying $x(t_0) = x_0$ also satisfies $x(t_1) = x_1$.

By solving (20) using variation of parameter method, with $\ddot{\mathrm{I}}^a(t, t_0)$ be the transition matrix of the homogeneous system $\dot{x}(t) = A(t)x(t)$. The solution is obtained as

$$x(t) = \ddot{\mathrm{I}}^a(t, t_0) + \int_{t_0}^{t} \ddot{\mathrm{I}}^a(t, \tau) B(\tau) u(\tau) d\tau \tag{21}$$

The system is controllable if and only if for arbitrary initial, x_1 and final states x_0, there exists a control function u such that;

$$x_1 = \ddot{\mathrm{I}}^a(t_1,t_0)x_0 + \int_{t_0}^{t_1} \ddot{\mathrm{I}}^a(t,\tau)B(\tau)u(\tau)d\tau \tag{22}$$

Based on the definitions 1 and 2, (20) is controllable, if x_0 is steered to x_1. Let's define $w_0 = x_0 - \ddot{\mathrm{I}}^a(t_0,t_1)x_1$, then there exist u, such that

$$0 = \ddot{\mathrm{I}}^a(t_1,t_0)w_0 + \int_{t_0}^{t_1} \ddot{\mathrm{I}}^a(t_1,\tau)B(\tau)u(\tau)d\tau \tag{23}$$

$$= \ddot{\mathrm{I}}^a(t_1,t_0)(x_0 - \ddot{\mathrm{I}}^a(t,t_0)x_1) + \int_{t_0}^{t_1} \ddot{\mathrm{I}}^a(t_1,\tau)B(\tau)u(\tau)d\tau \tag{24}$$

$$= \ddot{\mathrm{I}}^a(t_1,t_0)x_0 - x_1 + \int_{t_0}^{t_1} \ddot{\mathrm{I}}^a(t_1,\tau)B(\tau)u(\tau)d\tau \tag{25}$$

$$\therefore x_1 = \ddot{\mathrm{I}}^a(t_1,t_0)x_0 + \int_{t_0}^{t_1} \ddot{\mathrm{I}}^a(t_1,\tau)B(\tau)u(\tau)d\tau = x(t_1) \tag{26}$$

Equation (21) and, by implication, (26) hold if the system matrices A and B satisfies (27). By observing (10), it can be deduced that the system matrices have satisfied the condition, and therefore the system developed is controllable.

$$rank\begin{bmatrix} B & AB & A^2B & A^{n-1}B \end{bmatrix} = n \tag{27}$$

Definition 3. (Stabilizability): A linear time invariant control system in (19) is stabilizable if there exists a matrix $K \in \mathbb{R}^{m\times n}$ such that A + BK is a stability matrix.

It is established that (20) is controllable, hence, the controllability grammian matrix is defined as;

$$\mathscr{G}_T = \mathscr{G}(0,T) = \int_0^T e^{-At}BB^*e^{-A^*t}dt \tag{28}$$

The system in (20) is stabilizable if the grammian matrix, $\mathbf{G}_\mathrm{T}$ is positive for $T > 0$. From the feedback control law defined for the LQR controller in (19),

$$u(t) = -Kx(t) = -B^*\mathscr{G}_T^{-1}x(t) \tag{29}$$

It can be shown that u stabilizes (19)

$$A\mathscr{G}_T + \mathscr{G}_T A^* = \int_0^T \left\{Ae^{-At}BB^*e^{-A^*t} + e^{-At}BB^*e^{-A^*t}A^*\right\}dt \tag{30}$$

$$= \int_0^T \frac{d}{dt}\left\{e^{-At}BB^*e^{-A^*t}\right\}dt \tag{31}$$

$$= -e^{-At}BB^*e^{-A^*T} + BB^* \tag{32}$$

Rewriting (32) as,

$$\left(A - BB^*\mathscr{G}_T^{-1}\right)\mathscr{G}_T + \mathscr{G}_T\left(A - BB^*\mathscr{G}_T^{-1}\right)^* + e^{-At}BB^*e^{-A^*t} + BB^* = 0 \tag{33}$$

Implying that $\mathscr{G}_T$ is positive for $T > 0$. From (33), it can be intuitively shown that

$$e^{-At}BB^*e^{-A^*t} + BB^* \geq BB^*$$

Hence, $\left(A - BB^*\mathscr{G}_T^{-1}\right)$ and $\left(A - BB^*\mathscr{G}_T^{-1}\right)^*$ are stability matrices, indicating that the developed system in (19) is stabilizable by the control signal from the LQR controller.

3.2. Lower control layer

It is at this control level that the frequency and tie-line power are controlled by applying the supplementary control action signal to the generators. The PI controllers at this control level generates the control signal, P_i^{sc} for each area.

It worth noting that smaller values of the controller gains, K_i and K_p lead to slow system performance, while higher values causes excessive oscillations in the responses which results to instability. Hence, there is need to optimize the gains for better performance. As such, Moth Flame Optimization (MFO) (discussed in the next sub-section) is applied to tune the controllers based on the ISE criteria as shown in (34).

$min(J_i)$ Such that,

$$J_i = \int_0^t \left(u_i^{ref} - ACE_i\right)^2; \quad i = 1,\ 2,\ 3 \tag{34}$$

The ISE criterion is chosen for the controller design in order to curtail the effect of large initial errors and minimize the control effort. The

3.2.1. Constraints implementation

Owing to the mechanical components of the turbine, the rate of the change of the mechanical power owing to the change in the control signal, P^{sc} is limited to a certain range. This rate defined as Generation Rate Constraint (GRC) can adversely impair on the performance and stability of the control system. As such, for m th turbine in the ith CA, the GRC is modelled as;

$$GRC_{i,m} = \left|\frac{P_{i,m}^{sc} - P_{i,m}^{Gov}}{T_{T_{i,m}}}\right| \tag{35}$$

Since both $P_{i,m}^{sc}$ and $P_{i,m}^{Gov}$ are state variables of the augmented model, the GRC is implemented by imposing the limits on these variables. The GRC of typical thermal unit is normally taken as 10 %/min, and is therefore used in this study, defined as

$$GRC_{i,m} \leq 1.7 \times 10^{-3} pu/s \forall i,m \tag{36}$$

In addition, the fluctuation in the frequency is bounded within a predefined limit, f_i^{lim} in order to maintain the quality of the supply, as defined in (37).

$$|f_i| \leq f_i^{lim} : \forall i \tag{37}$$

Similarly, for physical consideration, the PI controller gains; K_{Pi} and K_{Ii} are equally bounded within certain limits, as shown in (38) and (39);

$$K_{Pi}^{min} \leq K_{Pi} \leq K_{Pi}^{max}; \tag{38}$$

$$K_{Ii}^{min} \leq K_{Ii} \leq K_{Ii}^{max}; \tag{39}$$

The local PIs in the lower level then generate the control signal for each area, using (40).

$$u_i = K_{Pi}\mathrm{ACE}_i(t) + K_{Ii}\int_0^t \mathrm{ACE}_i(t)dt; i = 1,2,3 \tag{40}$$

The system model as well as the controllers are discretized with a sample interval, T_s.

3.2.2. Moth Flame Optimization (MFO) algorithm

Generally, the framework of population-based algorithms is nearly undistinguishable. They involve generating a set of arbitrary initial solutions. Based on a predefined cost function and objective value, these initial solutions are evaluated to generate another candidate solutions. The algorithm then treats and updates these solutions via the fitness values for their improvement. The newly generated solutions are once more evaluated using the cost function and allocated their appropriate fitness values. The procedure is repeated iteratively till a predefined stoppage criterion is accomplished. Finally, the best among the candidate solutions is found and returned as the global optimum solution

[47,15]. Moth flame optimization (MFO) algorithm is not an exception.

MFO algorithm is one of the biologically inspired population-based optimization algorithms. MFO is inspired by the transverse orientation, spiral flying route of moths around artificial lights. The candidate solutions and the variables are the moths and their position in the space respectively. The movement of the moths in the space can be single, double or multi-dimensional, by adjusting the position vectors. For formulation sake, the set of moths are presented in a matrix form as in (41):

$$M = \begin{pmatrix} m_{11} & m_{12} & \cdots & m_{1v} \\ m_{21} & m_{22} & \cdots & m_{2v} \\ \vdots & \vdots & \ddots & \vdots \\ m_{n1} & m_{n2} & \cdots & m_{nv} \end{pmatrix} \tag{41}$$

With n representing the population of the moths, while v denotes the number of variables. For any set of moths, a special array ($\alpha_1, \alpha_2 \ldots \alpha_n$) is devoted to storing the set's fitness values. The fitness value in this regard refers to the selected value of the cost function for every single moth. Similarly, the flames are also denoted by a matrix with same size as that of the moth, as in (42):

$$F = \begin{pmatrix} F_{11} & F_{12} & \cdots & F_{1v} \\ F_{21} & F_{22} & \cdots & F_{2v} \\ \vdots & \vdots & \ddots & \vdots \\ F_{n1} & F_{n2} & \cdots & F_{nv} \end{pmatrix} \tag{42}$$

In the same vain, an array (F_1, $F_2 \ldots F_n$) is defined for the storage of the corresponding fitness values of all the flames. Both moths and flames are solutions, however the former are definite search agents that hover within the search space, while the latter indicate the best position of moths. With aid of this set of rules, none of the moth miss its best solution [21].

Moth Flame Optimization hinged on three key variables which execute the basic steps involved. Fundamentally, MFO is expressed as

$$MFO = (I, P, O) \tag{43}$$

Where I is a function used to randomly generate n number of moths and their respective fitness values. Whereas the actual function, P flies the moths within the search space. The matrix M is received by function P and return its updated one at the end of the iteration. For details on the background of MFO, [21]is recommended.

The pre-setting of some of the MFO parameters (population of the moths, and the number of variables) is done by considering the number of gains of the lower control layer PI controllers. In this regards, the variables are 6 in number ($K_{Pi}, K_{Ii}; i = 1, 2, 3$). While the rest; the light intensity, attraction coefficient and the maximum step size (maximum pace for each moth in a single iteration) are pre-set empirically.

To implement the optimal state feedback control, full state information need to be available to the controller. In this study, the state variables; f_i, P_i^{tie} and P_i^{SC} are taken as the accessible states in the ith CA, and therefore used by the KF to estimate the rest of the states for the LQR.

The LQR controller is chosen due to its;

(i) *Robustness*; LQR attains infinite gain-margin and ensures phase margin, and therefore implies good robustness.
(ii) *Stability*; with all the state information of the system are available and the system is well-modeled, then the stability margins are guaranteed.
(iii) *Automation*; the controller is automatically generated by simply selecting a couple of parameters devoid of loop-shaping.

The flowchart depicting the proposed LQR-PI based LFC is shown in Fig. 3.

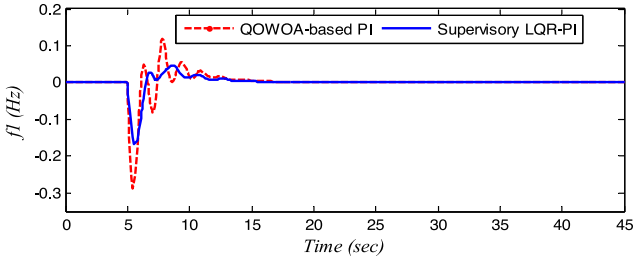

Fig. 4. f_1 with SD in CA_1.

4. Results and discussion

To investigate the efficacy and superiority of the proposed LFC scheme over conventional dec-PI LFC scheme, the three-area interconnected system developed is subjected to two different net disturbances. The system is then simulated in MATLAB (R2016a) environment. The system parameters used in the simulation are summarized in Table 2. The load disturbances comprised of single area step load change and multi-area random load changes.

4.1. Step net disturbance

To study the system responses following a step disturbance (SD) and evaluate its steady state characteristics, the aggregate of changes in the load demand and the RES in CA_1 is set to a step change of $0.1pu$. Net disturbance is applied at $t = 5\ s$ of the simulation time to ensure that no residual responses exist in the system. While the net changes in CA_2 and CA_3 are maintained constant. The control signal is constrained to $P_{i,m}^{sc} \leq 0.015pu$, and its update time is taken to be $2sec$. The responses of the states obtained with the supervisory LQR-PI control are analyzed and compared with conventional dec-PI control scheme.

The settling times, under/overshoots and ISEs of the states' deviations are used as the performance metrics. This is to weigh the effectiveness of the scheme in reducing the settling and rise times in order to mitigate the adverse consequence of wide initial errors and small long-lasting errors.

The ISE and ITAE of the states as well as the optimal controller gains obtained using the proposed QOWOA and other algorithms applied in some studies are summarized in Table 3. Figs. 4 – 6 show the close-loop responses of the frequency changes in CA_1 to CA_3 obtained with the proposed supervisory LQR-PI and QOWOA-tuned PI. It is evident from the responses that f_1 has larger undershoot in comparison to f_2 and f_3. This is an indication that CA_1 is the perturbed area.

Even though both control schemes stabilized the system states to their nominal values with near–zero steady state error, but the proposed supervisory LQR-PI scheme has slighter overshoot and settled the system

Table 2
Values of System Parameters.

Parameter	Value	Parameter	Value
β_1	$0.43puMW/Hz$	K_{T1}	$42.7puMW/Hz$
β_2	$0.41puMW/Hz$	K_{T2}	$56.8puMW/Hz$
β_3	$0.38puMW/Hz$	K_{T3}	$48.5puMW/Hz$
D_1	$2.25puMW/Hz$	T_{P1}	$22.5\ s$
D_2	$2.42puMW/Hz$	T_{P2}	$25.6\ s$
D_3	$2.28puMW/Hz$	T_{P3}	$24.2\ s$
R_1	$1.95puMW/Hz$	T_{T1}	$0.32\ s$
R_2	$1.84puMW/Hz$	T_{T2}	$0.30\ s$
R_3	$1.98puMW/Hz$	T_{T3}	$0.31\ s$
K_{P1}	$72.4puMW/Hz$	T_{Gov1}	$0.15\ s$
K_{P2}	$68.7puMW/Hz$	T_{Gov2}	$0.12\ s$
K_{P3}	$70.3puMW/Hz$	T_{Gov3}	$0.16\ s$
$\alpha_{12}, \alpha_{13}, \alpha_{23}$	1	T_s	$0.1\ s$
$f_i^{lim} : \forall i$	$0.2Hz$	$GRC_i : \forall i$	$\pm\ 0.1pu$/min

Table 3
Optimized PI gains and ISE.

	K_{i1}	K_{i2}	K_{i3}	K_{p1}	K_{p2}	K_{p3}	ITAE	ISE
WOA-based PI [39]	0.8648	0.615	0.990	0.880	0.990	0.0008	0.2320	9.82×10^{-4}
MFO-based PI [39]	0.9199	0.7890	0.587	0.655	0.943	0.168	0.2540	9.10×10^{-4}
dual mode PI [39]	0.5489	0.7278	0.5754	0.5899	0.880	0.945	0.1930	7.52×10^{-4}
QOWOA-based PI [7]	0.2445	0.5268	0.4552	0.6702	0.5803	0.6270	0.1855	7.23×10^{-4}
Supervisory MPC-PI [38]	0.0001	0.0020	0.0001	0.0470	0.0450	0.0460	–	–
Proposed Supervisory LQR	0.1240	0.2205	0.2549	0.3403	0.2629	0.3452	0.1542	4.68×10^{-4}

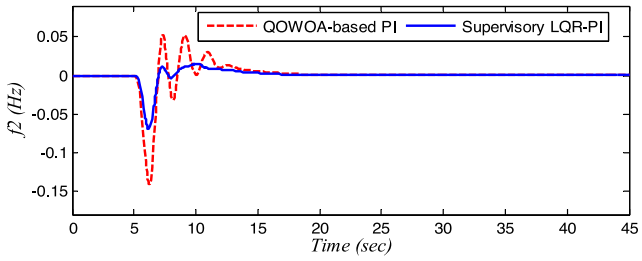

Fig. 5. f_2 with SD in CA_1.

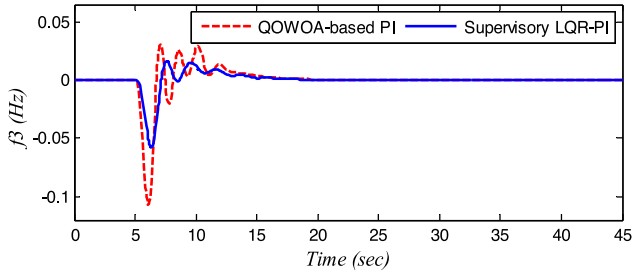

Fig. 6. f_3 with SD in CA_1.

Table 4
Over/Undershoots of frequency deviations with single area SLC.

Control Scheme	f_1		f_2		f_3	
	OS $\times 10^{-3}$	US $\times 10^{-3}$	OS $\times 10^{-3}$	US $\times 10^{-3}$	OS $\times 10^{-3}$	US $\times 10^{-3}$
WOA-based PI [39]	3.69	−15.4	1.9	−12.2	1.5	−10.5
MFO-based PI [39]	3.05	−15.6	2.3	−12.9	1.7	−11.4
Supervisory MPC-PI [38]	2.35	−11.2	2.12	−12.33	1.86	−13.46
QOWOA-based PI	2.29	−15.6	1.63	−13.1	1.94	−11.2
Proposed supervisory LQR	1.95	−6.88	1.38	−6.43	1.22	−6.88

faster, compared to the QOWOA-PI. In the same vain, the proposed scheme has outperformed the other techniques considered for comparison in this work, as summarized in Table 4. This is due to the coordinated control action and excellent constraints handling of the proposed scheme.

Despite the ability of the QOWOA-PI control scheme to stabilize the system, there noticeable oscillations in the responses. With the introduction of the LQR in the higher control layer which optimally set the references for the PIs in the lower layers, the oscillations are damped faster. Table 4 summarizes the performance of the proposed control scheme compared to other approaches.

By comparing the responses obtained using the proposed scheme

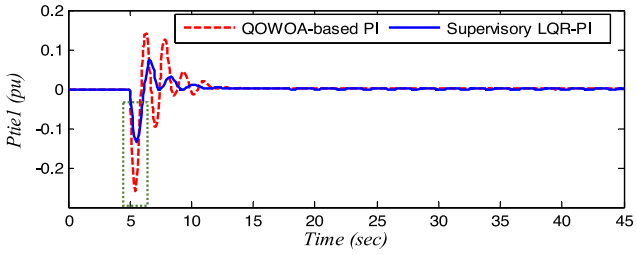

Fig. 7. P_1^{tie} with SD in CA_1.

with those obtained using QOWOA, a reduction of 16.15 %, 15.33 % and 15.46 % are observed in the overshoots of the frequency deviations of the CAs respectively. This indicates an improved dynamic response of the proposed supervisory LQR over the decentralized scheme.

Fig. 7 shows the response of tie-line power deviation of CA_1 following the net disturbance (step), P_1^{net} of $0.1pu$ with the proposed supervisory LQR and dec-PI control. From the response, the developed supervisory LQR controller settled the tie line power response faster with reduced oscillations in comparison with the dec-PI scheme. Similar improvements can be observed in P_2^{tie} and P_3^{tie} shown in Figs. 8 and 9 respectively. The undershoot observed in P_1^{tie} indicates that the net disturbance occurred in CA_1 and power flows into that CA during the transients. Similarly, the overshoots in P_2^{tie} and P_3^{tie} indicate the outflow of power flow from CA_2 and CA_3 to the disturbed CA_1.

The overshoots of the tie-line power deviations, summarized in Table 5, are observed to have reduced by 20.27 %, 22.5 % and 21.76 % in the three respective areas, when compared with the QOWOA-based dec-PI scheme. This demonstrates the superior performance of the supervisory LQR over the dec-PI control and other schemes.

The improvements in the dynamic responses is not only noticeable in the over/undershoots of the responses, but also in their settling times. Table 6 summarizes the settling times of the deviations in the three control areas obtained from the proposed control scheme compared with other schemes.

Following the disturbance, the frequency-responsive spinning reserves respond by adjusting their output powers according to the new P_i^{sc}. However, to preserve the vertically integrated utility characteristics of the system, zero inter-CA power flows among the CAs need to be maintained. As such, at steady state, only the generator(s) in the perturbed area balance up the net disturbance. This is established from the

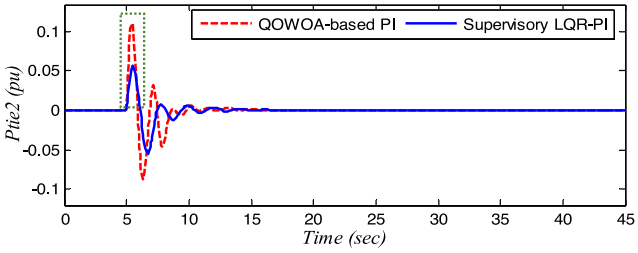

Fig. 8. P_2^{tie} with SD in CA_1.

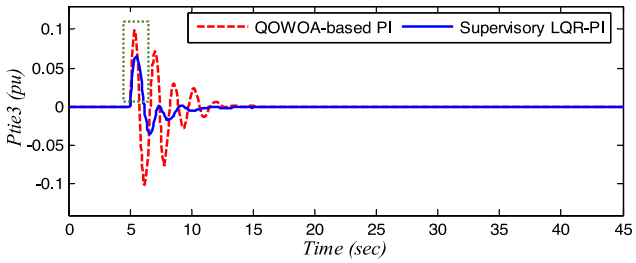

Fig. 9. P_3^{tie} with SD in CA_1.

Table 5
Over/Undershoots of tie-line power deviations with single area SLC.

Control Scheme	$P_1^{tie}(pu)$		$P_2^{tie}(pu)$		$P_3^{tie}(pu)$	
	OS $\times 10^{-3}$	US $\times 10^{-3}$	OS $\times 10^{-3}$	US $\times 10^{-3}$	OS $\times 10^{-3}$	US $\times 10^{-3}$
WOA-based PI [39]	1.91	−7.1	3.5	−1.2	3.5	−4.6
MFO-based PI [39]	2.20	−7.3	3.6	−1.2	3.4	−3.4
QOWOA-based PI	1.48	−7.2	3.6	−1.15	3.4	−2.2
Proposed supervisory LQR	1.18	−4.56	2.79	−1.05	2.66	−1.84

Table 6
Settling Times of the frequency and tie-line power deviations.

	f_1	f_2	f_3	P_1^{tie}	P_2^{tie}	P_3^{tie}
hGSA–PS: PI [37]	14.66	13.65	13.67	14.14	11.23	12.09
QODSA-based PI [7]	6.65	9.60	9.59	11.02	9.05	11.78
WOA-based PI [39]	10.0	9.5	10.3	6.49	9.9	10.2
MFO-based PI [39]	11.60	11.0	11.5	15.5	7.5	10.5
QOWOA-based PI	8.45	8.0	8.20	5.8	6.1	8.0
Proposed supervisory LQR-PI	6.59	6.18	6.37	4.55	4.86	6.29

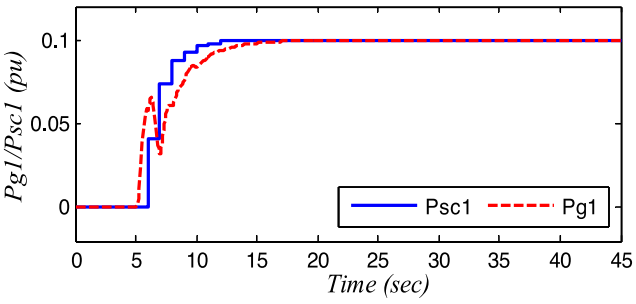

Fig. 10. P_1^G and P_1^{sc} with SD in CA_1.

response of the generators shown in Figs. 10 – 12. The responsive generators (spinning reserve) in CA_1 generates the load change of $0.1pu$ at steady state, while the generators in the other CAs settle at zero.

4.2. Multi-area random disturbances.

Frequency fluctuations in power system is not only caused by change in loads but also fluctuations from the generation sides, particularly the RES. The output power of RES is characterized by excessive fluctuations, which in turn led to frequency instability. In this subsection, the effectiveness of the supervisory LQR control scheme in stabilizing the system under a continuous and random disturbance (RD) is demonstrated. The

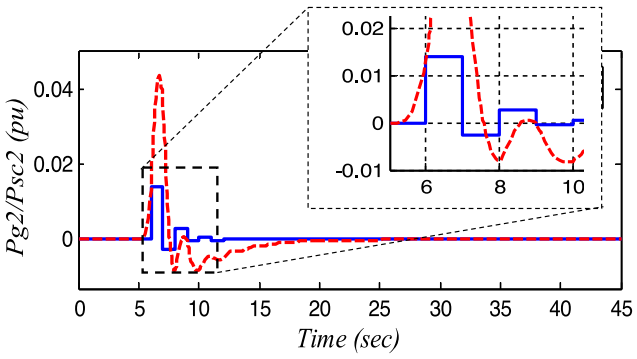

Fig. 11. P_2^G and P_2^{sc} SD in CA_1.

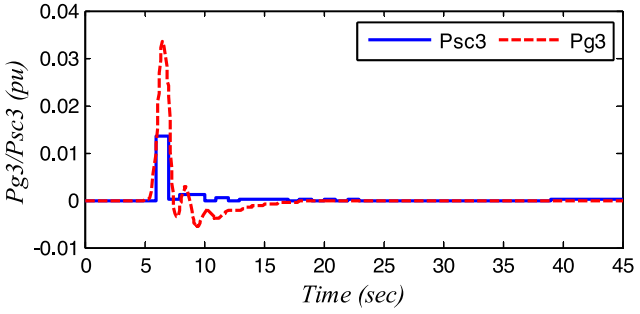

Fig. 12. P_3^G and P_3^{sc} with SD in CA_1.

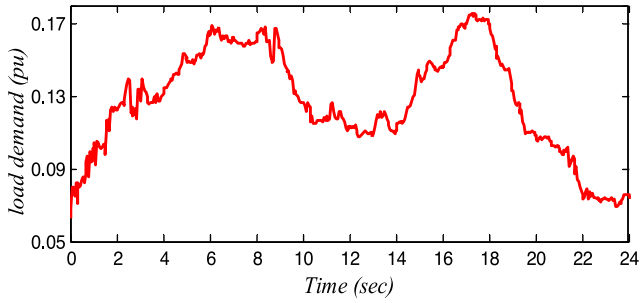

Fig. 13. Random load perturbation profile.

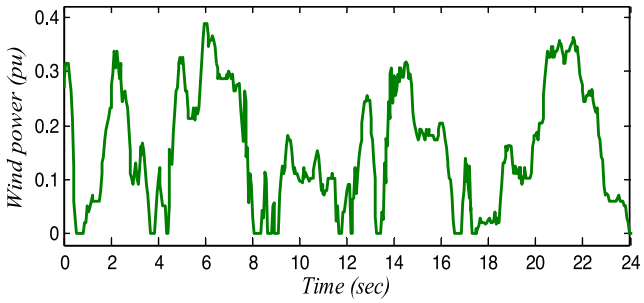

Fig. 14. DFIG-based WT Power.

net disturbance is obtained using (2) with the random load change shown in Fig. 13 and fluctuations from RES (DFIG-based wind turbine generator) power with profile in Fig. 14. To some extent, the net disturbance represents a real-life scenario. The control signal is constrained as $P_{i,m}^{sc} \leq 0.015pu$.

The wind power model is obtained based on Ornstein-Uhlenbeck

Table 7
Statistical properties of the wind power and load demand.

Disturbance	Min	Max	Average	Standard dev.
Wind power (pu)	0	0.3863	0.1543	0.1094
Load demand (pu)	0.067	0.1755	0.1272	0.0286

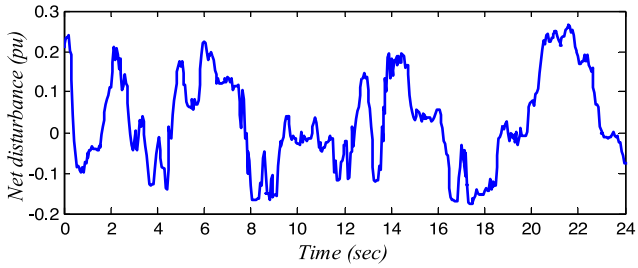

Fig. 15. Net disturbance to the system.

Geometric Brownian Motion model presented in [17]. The statistical properties of the random load and the WT power is summarized in Table 7

The resultant effect of these two disturbances, shown in Fig. 15 is applied to CA_1 and CA_3 while keeping CA_2 steady.

The Kalman filter (KF) estimates the inaccessible states based on the measurable ones. In addition, its covariance matrices, Q_{kf} and R_{kf} are adjusted depending on the continuous values of the noises; ξ and ψ.

It can be observed from the trajectories of the frequencies depicted in Figs. 16–18, both control schemes stabilize the frequency fluctuations, however the supervisory LQR scheme constrained the deviation within the $\pm$ 0.2 Hz limits. The failure of the QOWOA-PI to maintain the frequency with the allowable limit demonstrated its deficiency in handling the constraints, uncertainties and nonlinearities in the system.

Similar performance is observed in the dynamic responses of the tie-line powers shown in Figs. 19–21.

It is also demonstrated that the supervisory LQR scheme is not only capable of regulating the frequency following a single area disturbance as in the first scenario, but also in multiple areas. This is certainly due to the coordination of the LQR at the higher layer offered to the control actions of the decentralized local PIs in the lower layer. Table 8

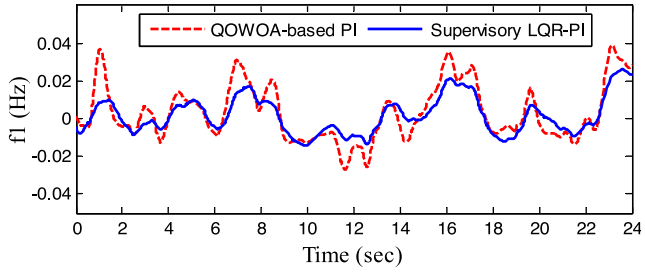

Fig. 16. f_1 with RD in CA_1 and CA_3.

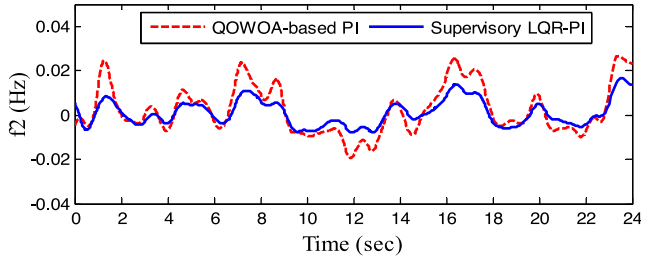

Fig. 17. f_2 with RD in CA_1 and CA_3.

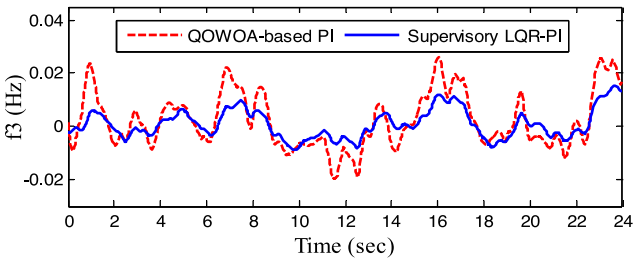

Fig. 18. f_3 with RD in CA_1 and CA_3.

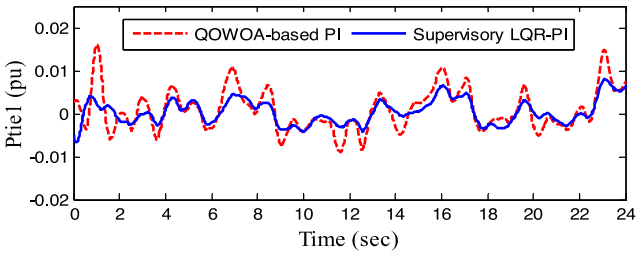

Fig. 19. P_1^{tie} with RD in CA_1 and CA_3.

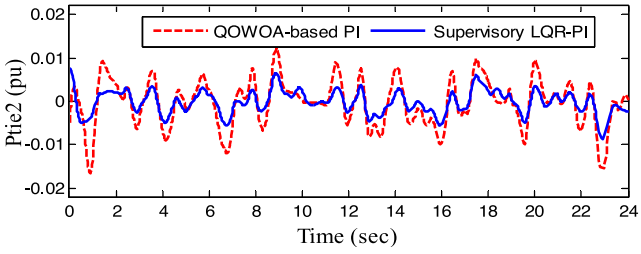

Fig. 20. P_1^{tie} with RD in CA_1 and CA_3.

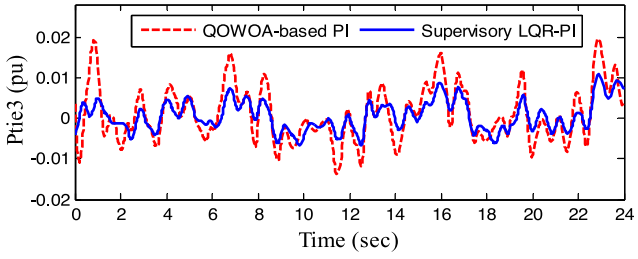

Fig. 21. P_3^{tie} with RD in CA_1 and CA_3.

summarizes the ISE of the responses.

By observing the trajectory of the CA_2 generators' response shown in Fig. 22, it can be seen that the GRCs have been adequately handled. This reveals the remarkable performance of proposed control scheme devoid of violating the system constraints.

5. Conclusion

In this paper, a control scheme with bi-level hierarchical structure is

Table 8
ISE of the ACE following RD in CA_1 and CA_3.

Areas	ISE (pu^2)
CA_1	2.744×10^{-4}
CA_2	5.134×10^{-5}
CA_3	1.125×10^{-4}

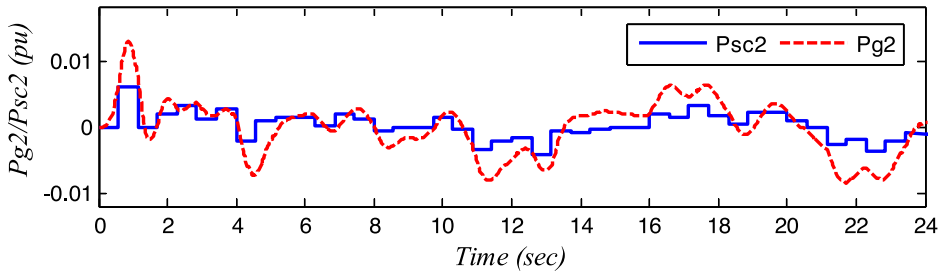

Fig. 22. P_2^G and P_2^{sc} with RD in CA_1 and CA_3.

proposed for LFC. In the upper level of the control, an LQR is applied to determine the set points of PI controllers in the lower control level. The PI controllers, installed in each of the three CAs of the interconnected system, regulate the frequencies and tie-line powers. The close loop performance of the proposed control scheme is improved by optimizing the gains of the local PI controllers considering the local information of each CA and its interactions with the neighboring CAs. Kalman filter (KF) is applied as an observer to estimate all the unmeasurable states of the system while its covariance matrices were adjusted considering the variation of the noises in the states. The system is subjected to step and random time-varying net disturbances. The simulations carried out demonstrated the superior performance of the proposed LQR-PI scheme compared conventional PI control scheme in optimality, stability and constraints handling.

Declaration of Competing Interest

The author declares that he has no known competing financial interests or personal relationships that could have appeared to influence the work reported in this paper.

Data availability

Data will be made available on request.

References

[1] Ali E. Design of PSO-Based Fuzzy Gain Scheduling PI Controller for Four-Area Interconnected AGC System after Deregulation. King Saud Univ J, Eng Sci. 1419/1999;1:49–69.
[2] Ansari J, Abbasi AR, Firouzi BB. Decentralized LMI-based event-triggered integral sliding mode LFC of power systems with disturbance observer. Int J Electr Power Energy Syst 2022;138:1–11.
[3] Azeer SA, Ramjug-Ballgobin R, Hassen SZS. Intelligent Controllers for Frequency Control for Two Area Power System. Mauritius: Réduit; 2017.
[4] Chidambaram IA, Velusami S. Design of Decentralized Biased Controllers for Load-Frequency Control of Interconnected Power Systems. Electr Power Compon Syst 2005;33:1313–31.
[5] Ejegi E, Rossiter JA, Trodden P. Distributed model predictive load frequency control of a deregulated power system. Belfast, UK., UKACC 11th International Conference on Control (CONTROL) 2016.
[6] Ersdal AM, Imsland L, Uhlen K. Model Predictive Load-Frequency Control. IEEE Trans Power Syst 2016;31(1):777–85.
[7] Guha D, Roy PK, Banerjee S. Quasi-oppositional differential search algorithm applied to load frequency control. Eng Sci Technol, Int J 2016;19(4):1635–54.
[8] Gupta BR. Power System Analysis and Design. New Delhi: S. Chand Publishing; 2008.
[9] Hota P, Mohanty B. Automatic generation control of multi source power generation under deregulated environment. Electr Power Energy Syst 2016;75:205–14.
[10] Khan M, Sun H, Xiang Y, Shi D. Electric vehicles participation in load frequency control based on mixed H2/H∞. Int J Electr Power Energy Syst 2021;125.
[11] Kumari N, Jha AN. Automatic Generation Control Using LQR based PI Controller for Multi Area Interconnected Power System. Adv Electron Electric Eng 2014;4(2):149–54.
[12] Kunya AB, Argin M. Model Predictive Load Frequency Control of Multi-Area Interconnected Power System. Texas, USA: College Station; 2018.
[13] Kunya AB, Argin M, Kucuksari S. Optimal Load Frequency Control of Multi-Area Power System Considering Incremental Control Action. Texas, USA, s.n.: College Station; 2019.
[14] Kunya AB, Argin M, Sha'aban YA, Jibril Y. Coordinated Load Frequency and Voltage Control of Multi-Area Power System. Beni-Suef University. J Basic Appl Sci. 2020;9.
[15] Lee HM, Jung D, Sadollah A, Lee EH. Performance Comparison of Metaheuristic Optimization Algorithms Using Water Distribution System Design Benchmarks. In: Harmony Search and Nature Inspired Optimization Algorithms Theory and Applications. Warsaw, Poland: Springer; 2019. p. 97–104.
[16] Liu X. Event-triggering load frequency control for multi-area power system based on random dynamic triggering mechanism and two-side closed functional. ISA Trans Issue 2022. https://doi.org/10.1016/j.isatra.2022.06.028.
[17] Loukatou A, Howell S, Johnson P, Duck P. Stochastic wind speed modelling for estimation of expeccted wind power output. Appl Energy 2018;228:1328–40.
[18] Luis MC. Simulation framework for automatic load frequency control studies of VSC-based AC/DC power grids. Electric Power Energy Syst 2022;141:1–11.
[19] Ma M, Zhang C, Liu X, Chen H. Distributed Model Predictive Load Frequency Control of Multi-Area Power System after Deregulation. IEEE Trans Ind Electron 2017;64(6):5129–39.
[20] Mehta P, Bhatt P, Pandya V. Optimized coordinated control of frequency and voltage for distributed generating system using Cuckoo Search Algorithm. Ain Shams Eng J 2017;23:1–10.
[21] Mirjalili S. Moth-Flame Optimization Algorithm: A Novel Nature-inspired Heuristic Paradigm, Knowledge-Based Systems. Knowl-Based Syst. 2015;89:228–249. http://dx.doi.org/10.1016/j.knosys.2015.07.006.
[22] Mohamed TH, Shabib G, Abdelhameed EH, Khamies M. Load Frequency Control in Single Area System Using Model Predictive Control and Linear Quadratic Gaussian Techniques. Int J Electr Energy 2015;3(3):141–3.
[23] Nelem A. An application of multicriteria decision aid in switching state control of hybrid electric power generation network. King Saud Univ J, Eng Sci. 2021;1–12. http://doi.org/10.1016/j.jksues.2021.05.005.
[24] Pradhan C, Bhende CN. Online load frequency control in wind integrated power systems using modified Jaya optimization. Eng Appl Artif Intel 2019;77:212–28.
[25] Prasada S, Purwar S, Kishor N. Load frequency regulation using observer based non-linear sliding mode control. Electr Power Energy Syst 2019;104:178–93.
[26] Rahmani M, Sadati N. Hierarchical optimal robust load-frequency control for power systems. IET Gener Transm Distrib 2012;6(4):303–12.
[27] Rahmani M, Sadati N. Two-level optimal load–frequency control for multi-area power systems. Electr Power Energy Syst 2013;53:540–7.
[28] Rahman M, Sarkar SK, Das SK. Stabilization Improvement of Load Frequency Deviation for Multi-Area Interconnected Smart Grid Using Integral Linear Quadratic Gaussian Control Approach. Dhaka: Bangladesh, s.n; 2018.
[29] Sahoo DK, Sahu RK, Sekhar C, Panda S. A novel modified differential evolution algorithm optimized fuzzy proportional integral derivative controller for load frequency control with thyristor controlled series compensator. J Electr Syst Inform Tech 2018;5:944–63.
[30] Sahu PC, Mishra S, Prusty RC, Panda S. Improved -salp swarm optimized type-II fuzzy controller in load frequency control of multi area islanded AC microgrid. Sustain Energy Grids Netw 2018:1–28. https://doi.org/10.1016/j.segan.2018.10.003.
[31] Santosh T, Vijay PS, Nand K, Pandey AS. Load frequency control of power system considering electric Vehicles' aggregator with communication delay. Int J Electr Power Energy Syst 2023;145:1–10.
[32] Sariki M, Shankar R. Optimal CC-2DOF(PI)-PDF controller for LFC of restructured multi-area power system with IES-based modified HVDC tie-line and electric. Eng Sci Technol, Int J 2022;32:1–15.
[33] Satapathy P, Singh MB, Debnath MK, Mohanty PK. Design of FPI controller for Load Frequency control of a Nonlinear Power System. India, s.n.: Bhubaneswar; 2018.
[34] Saxena A, Shankar R. Improved load frequency control considering dynamic demand regulated power system integrating renewable sources and hybrid energy storage system. Sustain Energy Technol Assess 2022;52(C):1–19. https://doi.org/10.1016/j.seta.2022.102245.
[35] Saxena S. Load frequency control strategy via fractional-order controller and reduced order modelling. Electr Power Energy Syst 2019;104:603–14.
[36] Shahalamia SH, Farsi D. Analysis of Load Frequency Control in a restructured multi-area power system with the Kalman filter and the LQR controller. Int'l J Electron Commun 2018;86:25–46.
[37] Sharma Y, Saikia LC. Automatic generation control of a multi-area Thermal power system using Grey Wolf Optimizer algorithm based classical controllers. Electr Power Energy Syst 2015;73(2):853–62.

[38] Shiroei M, Ranjbar AM. Supervisory predictive control of power system load frequency control. Electr Power Energy Syst 2014;61:70–80.
[39] Simhadri KS, Mohanty B. Performance analysis of dual-mode PI controller using quasi-oppositional whale optimization algorithm for load frequency control. Int Trans Electr Energy Syst 2019:1–23.
[40] Solheim OA. Design of optimal control systems with prescribed eigenvalues. Int J Control 1972;15(1):143–60.
[41] Stil VJ, Mehmedovic M. Interconnection and damping assignment automatic voltage regulator for synchronous generators. Electr Power Energy Syst 2018;101: 204–12.
[42] Wadhwa CL. Electrical power systems. New Delhi, India: New Age Int'l limited Publishers; 2010.
[43] Warrier BR, Vijayakumari A, Kottayil SK. Dynamic adaptability of model predictive control for power converters in inverter dominated microgrids. King Saud Univ J Eng Sci 2019;34:260–72.
[44] Xia C, Liu H. Bi-Level Model Predictive Control for Optimal Coordination of Multi-Area Automatic Generation Control Units under Wind Power Integration. Processes 2019;7(666):1–19. http://doi.org/10.3390/pr7100669.
[45] Yang L, Liu T, Hill DJ. Distributed MPC-based frequency control for multi-area power systems with energy storage. Electr Pow Syst Res 2021;190:1–7.
[46] Yang S, Huang C, Yu Y, Dong X. Load Frequency Control of Interconnected Power System via Multi-Agent System Method. Electr Power Compon Syst 2017. https://doi.org/10.1080/15325008.2015.1131764, p. 1-13.
[47] Yang X-S. Nature-Inspired Optimization Algorithms. London: Elsevier; 2014.
[48] Zhang Y, Liu X, Qu B. Distributed Model Predictive Load Frequency Control of Multi-area Power System with DFIGs. IEEE/CAA J Automatica Sinica 2017;4(1): 125–35.
[49] Zhu F, Zhou X, Zhang Y, Fu DX. A load frequency control strategy based on disturbance reconstruction for multi-area interconnected power system with hybrid energy storage system. Energy Report, 2021;7:8849–8857. https://doi.org/10.1016/j.egyr.2021.09.029.